# CMS Draft Analysis Note

The content of this note is intended for CMS internal use and distribution only

2010/12/22

Head Id: 1.0

Archive Id: Archive Date:

# Search for Collimated Groups of Muons

Jim Pivarski, Alexei Safonov, Aysen Tatarinov

### **Abstract**

We present an inclusive, signature-based search for groups of collimated muons, arising from spectroscopic cascades in a hidden sector accessible only through high-energy collisions, using the CMS detector. In several signatures defined by number of muons per collimated group and number of groups per event, we searched for the lightest on-shell state in the hidden spectrum with a mass-peak fit and set limits on  $\sigma \mathcal{B} \alpha$ , where  $\alpha$  is the model acceptance of the signature. Depending on the signature and the mass of the lightest state  $(2m_{\mu}-5 \text{ GeV}/c^2)$ , new resonances are ruled out at the level of XX-YY pb for 95% C.L. We also set  $\sigma \mathcal{B}$  limits on two representative benchmark models: SUSY dark matter with a  $\mathcal{U}(1)_{\text{dark}}$  and NMSSM Higgs escaping LEP limits via Higgs-to-Higgs decays.

This box is only visible in draft mode. Please make sure the values below make sense.

PDFAuthor: CMS Collaboration

PDFTitle: Search for Collimated Groups of Muons

PDFSubject: CMS

PDFKeywords: CMS, physics, exotica, muons

Please also verify that the abstract does not use any user defined symbols



#### 1 Introduction

#### <sub>2</sub> 1.1 Motivation

FIXME: Needs a lot of references.

Although the dimuon mass spectrum is well understood in  $e^+e^-$  and  $p\bar{p}$  collisions up to collision energies of 0.2 and 2 TeV respectively, (FIXME: get real numbers) new states may be hidden by weak couplings to Standard Model particles. A wide class of hidden-valley models predicts new states coupling weakly to the Standard Model yet significantly to a hidden sector, accessible to the LHC through massive particles that connect the two sectors. In these scenarios, massive particles M would be created singly or in pairs and then decay through the hidden spectrum to the lightest hidden state:  $pp \to MM$  and  $M \to mX$  where m is the lightest hidden particle. If m is unstable, it would decay with very small width to the kinematically-accessible Standard Model 12 states, either democratically (Z-like) or to the heaviest accessible state (Higgs-like). Muon-pair final states would appear as a low-mass, high-momentum dimuon reso-14 nance, and therefore be collimated by relativistic boost. With several low-mass states in the decay chain, e.g.  $m_2 \to m_1 m_1 \to 4\mu$ , cascades would either produce two groups 16 of collimated dimuons or one group of four collimated muons, depending on the boost 17 of  $m_2$ . Arbitrarily complex decay chains are conceivable, and groups of muons might be produced in association with other Standard Model pairs, such as  $e^+e^-$  and  $\pi\pi$ . 19 These striking signatures are often called "lepton jets."

Hidden, low-mass resonances are especially interesting in light of the high-energy positron excess reported by the PAMELA primary cosmic-ray experiment. This ex-22 cess of interstellar positrons could be the product of WIMP annihilations, assuming that the WIMP annihilation rate is higher than what would be expected from thermal freeze-out in the early universe, and also assuming some mechanism to prohibit decay 25 chains that produce antiprotons, in which no excess was observed. A new force boson, 26  $z_{\rm dark}$ , with a mass of approximately 1 GeV/ $c^2$  and coupling significantly to WIMPs 27 yet weakly to Standard Model particles, would explain both observations. Acting as a long-range Yukawa force, z<sub>dark</sub> would draw together slow-moving WIMPs, increasing 29 their effective annihilation cross-section in the modern era without affecting their production in the early universe. As a decay channel,  $z_{\rm dark} \to p\bar{p}X$  would be kinematically 31 forbidden if the mass of  $z_{\text{dark}}$  were above 2 GeV/ $c^2$  or so. Relatively simple extensions 32 of this picture, such as adding a dark Higgs boson  $h_{dark}$  to give the  $z_{dark}$  its mass, or introducing the force with non-abelian structure, would produce more complex event topologies:  $2^N$  fermion pairs per lepton jet for a two-body decay chain with N light states and/or several lepton jets per event if the decay chain includes heavy particles. 36

Another, very different, motivation derives from the tension between the low Higgs mass predicted by precision electroweak fits and the direct LEP limit of 114 GeV/ $c^2$ . This limit assumes that the Higgs boson decays directly into Standard Model particles with known branching fractions. If additional light Higgs bosons allow for Higgs-to-

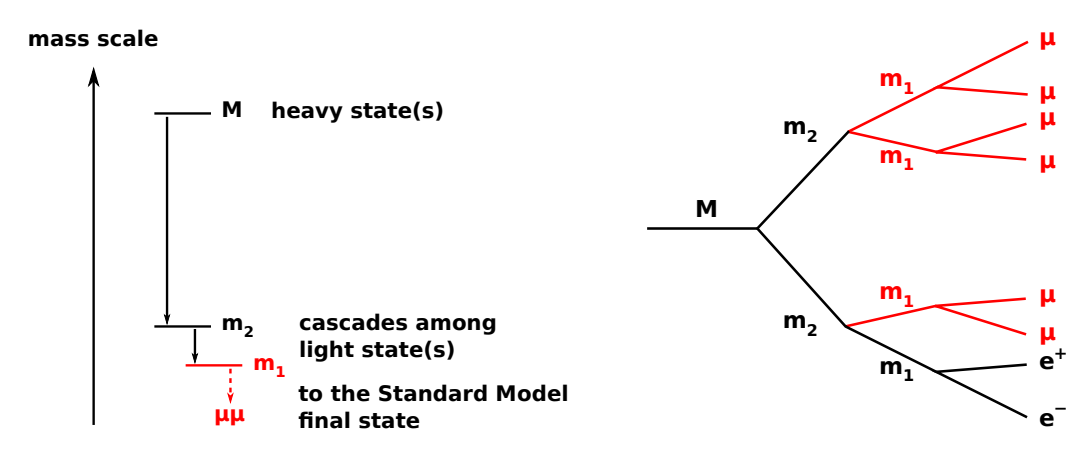


Figure 1: Schematic of a decay chain from heavy states in the hidden sector to light states, ultimately to Standard Model pairs. We identify groups of muons collimated by boost, possibly containing non-muons and search for a resonance in muon pairs from  $m_1 \rightarrow \mu\mu$ .

Higgs decays, the direct limit may be circumvented. In a well-defined region of Next-to Minimal SuperSymmetric (NMSSM) parameter space, the lightest CP-odd Higgs  $(a_1)$  can have arbitrarily low mass. Below the  $2m_{\tau}$  threshold, the branching fraction for  $a_1 \rightarrow \mu\mu$  is about 20%, making its detection in the muon channel visible. For values of the NMSSM parameters that give the lightest CP-even Higgs  $(h_1)$  a large singlet field component,  $h_1 \rightarrow a_1a_1$  can be as large as 100%. If nature has chosen this model, then the Higgs mass could be as low as  $86 \text{ GeV}/c^2$  and the primary Higgs signature would be  $h_1 \rightarrow a_1a_1 \rightarrow 2\mu, 2\mu$ , where the dimuons appear as well-collimated lepton jets.

#### 1.2 Method

In this paper, we present an inclusive, signature-based search for collimated dimuons with a  $2m_{\mu}$ –5 GeV/ $c^2$  resonance peak arising from hidden, on-shell cascade chains. Additional objects, such as isolated single leptons, hadronic jets, and missing energy, are neither included in the search nor are they forbidden. In particular, boosted dimuons are not rejected if they are overlapped by  $e^+e^-$  or  $\pi\pi$  from other resonance decays in the same lepton jet, nor are they rejected due to activity from a nearby hadronic jet that might arise, for example, from cascades of supersymmetric particles.

We assume that all decay chains in the hidden sector reach an on-shell lowest-mass state  $m_1$  before decaying to opposite-sign muon pairs, though there may be several instances of this particle per event, possibly overlapping one another (Fig. 1). This assumption is equivalent to assuming that the coupling between the hidden states and the Standard Model is much weaker than the couplings of the hidden states with each other, and the spectrum of heavy states is not highly degenerate. We therefore search for one new resonance with a single dimuon mass peak, after identifying the combination of muon pairs that is most likely to have arisen from distinct resonance decays.

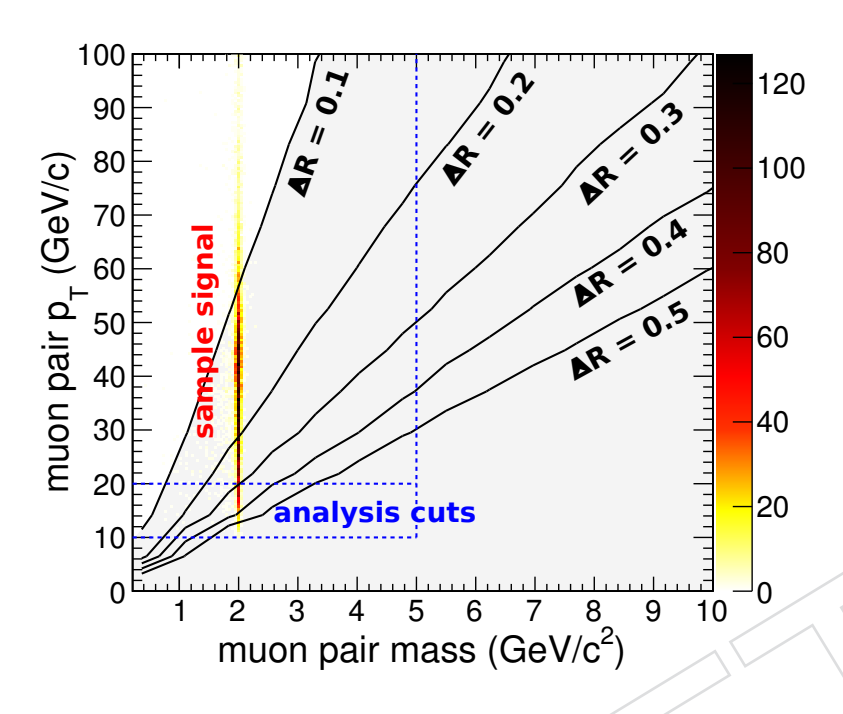


Figure 2: Sample signal (NMSSM with  $m_{h_1} = 100 \text{ GeV}/c^2$  and  $m_{a_1} = 2 \text{ GeV}/c^2$ ) on the momentum-mass plane, superimposed by dashed lines indicating analysis cuts and lines of constant  $\Delta R$  (for comparison only: not used to select mu-jets).

Identifying the distinct dimuon resonances proceeds in two steps. First, nearby muons are grouped into "mu-jets" with an arbitrary number of muons per group. The definition of "nearby muons" is kinematic rather than geometric: two muons are considered near each other if their pairwise invariant mass is less than  $5 \text{ GeV}/c^2$  with both muons satisfying a minimim- $p_T$  threshold. This differs from selections based on a maximum  $\Delta R = \sqrt{(\Delta \phi)^2 + (\Delta \eta)^2}$  because  $\Delta R$  approximately corresponds to relativistic boost, effectively a tighter requirement on resonance momentum for higher resonance masses (see Fig. 2).

The second step in identifying distinct dimuon resonances is to split high-multiplicity mu-jets into a combination of pairs with nearly equal mass for all pairs. For example, a mu-jet containing four muons from  $m_2 \to m_1 m_1 \to 4\mu$  has two potential combinations, and the combination with more nearly equal masses is much more likely to correspond to the true mass of  $m_1$ . This is illustrated in Fig. 3 with a sample signal in which  $m_2 = 3 \text{ GeV}/c^2$  and  $m_1 = 1 \text{ GeV}/c^2$ . We call the opposite-sign muon pairs after this step "fundamental dimuons," and there is only one candidate combination per event.

The number of mu-jets and the number of muons in each mu-jet is used to classify different signal topologies (any ungrouped muons are ignored). A separate mass-peak fit is performed in the N-dimensional fundamental dimuon spectrum of each signal topology, where N is the number of fundamental dimuons per event. These topologies

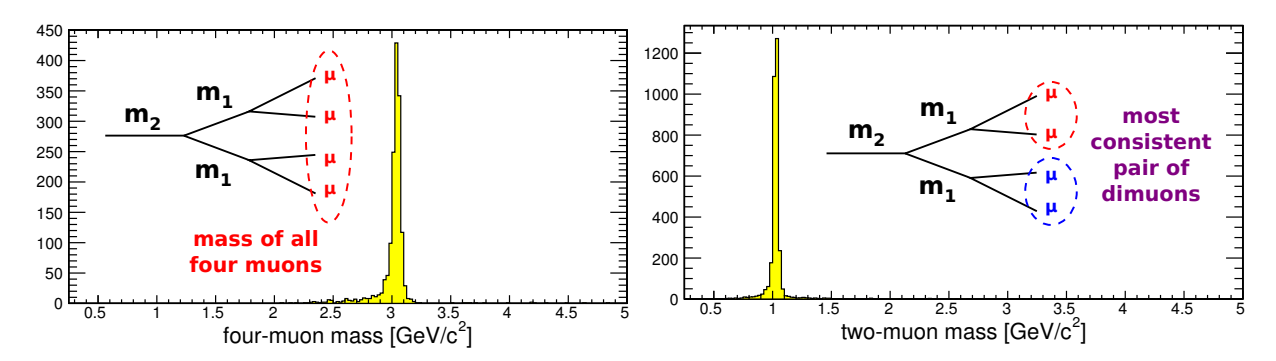


Figure 3: Identification of fundamental dimuons in a mu-jet containing four muons from  $m_2 \to m_1 m_1 \to 4\mu$ . The invariant mass of all four muons is a sharp peak at  $m_2$  (3 GeV/ $c^2$  in this example), and the invariant mass of the most consistent pair of dimuons within this mu-jet is a sharp peak at  $m_1$  (1 GeV/ $c^2$  in this example).

4 are:

85

86

87

88

89

90

91

92

93

94

95

96

97

98

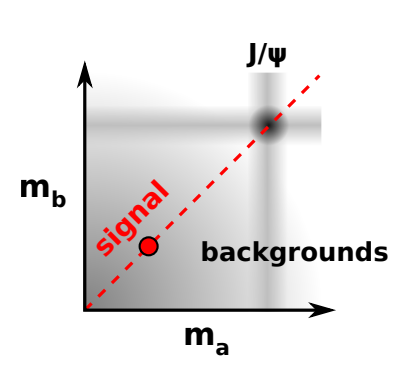
101

103

104

- (a) only one mu-jet per event:
  - (a-1) two muons in the mu-jet with vector-sum  $p_T > 80 \text{ GeV}/c$ , targeting models with a single high-momentum  $m_1 \to \mu\mu$ ,
  - (a-2) four muons in the mu-jet, targeting models with a low-mass  $m_2$  decaying via  $m_2 \rightarrow m_1 m_1 \rightarrow 4 \mu$ ,
  - (a-3) more than four muons in the mu-jet, for more complex models;
- (b) two mu-jets per event:
  - (b-1) each mu-jet contains exactly two muons, targeting a model with a heavy particle M decaying to two light particles  $m_1$ :  $M \to m_1 m_1 \to 4\mu$  (this is the NMSSM signature),
  - (b-2) one mu-jet contains two muons, the other contains four, targeting  $M \rightarrow m_1 m_2$  with  $m_1 \rightarrow \mu \mu$  and  $m_2 \rightarrow m_1 m_1 \rightarrow 4 \mu$ ,
  - (b-3) both mu-jets contain four muons for  $M \rightarrow m_2 m_2$ ,
  - (b-4) one mu-jet with more than four muons, for more complex models;
- (c) more than two mu-jets per event, targeting even more complex models.

Mass-peak fits are used to search for a narrow resonance above background, with the background normalization determined as a free parameter in the fit. The signal is modeled as a narrow Crystal Ball resonance determined by detector resolution and muon final state radiation, and the background shape is derived from a mass template in background control samples. In cases with two or more fundamental dimuons per event, the signal is constrained to the diagonal in which the mass of all fundamental



111

112

113

114

115

116

117

118

119

121

122

124

125

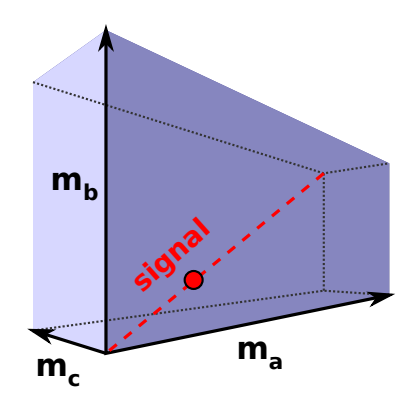


Figure 4: Schematic of multidimensional fits for a single  $m_1$  peak on Standard Model backgrounds. The peak must be located on the diagonal of the space, while the backgrounds are distributed throughout the space.

dimuons is nearly equal, while the background is more uniformly distributed through the space (Fig. 4). If an  $m_1$  mass peak is discovered in one of the topologies with two or more dimuons, then more complex fits will be performed to see if they belong to a cascade. A special 3-D fit to  $m_{h_1}$ ,  $m_{a_1}$ , and  $m_{a_1}$  is performed for the NMSSM case  $h_1 \rightarrow a_1 a_1 \rightarrow 2\mu$ ,  $2\mu$ .

To avoid introducing complicated model-dependent efficiencies, signal regions are defined by kinematic cuts that avoid trigger turn-on curves and regions where the detector loses efficiency for muons that are very close to one another. Within the predefined acceptance regions, the efficiency depends only on muon pseudorapidity  $\eta$ . In brief, the acceptance cuts that we use are

- at least one muon with  $p_T > 15 \, \text{GeV}/c$  and  $|\eta| < 0.9$  per event (muon barrel system trigger plateau);
- all other muons must have  $p_T > 5$  GeV/c and  $|\eta| < 2.4$  (offline reconstruction plateau).

The cuts on muon kinematics imply the following endpoints in mu-jet kinematics:

- at least one mu-jet with  $p_T > 20 \, {\rm GeV}/c$  and  $|\eta| \lesssim 0.9$  per event;
- all other mu-jets (if any) with  $p_T > 10 \text{ GeV}/c$  and  $|\eta| \lesssim 2.4$ .

The  $\eta$  endpoints on mu-jets are only tight in the limit of highly boosted mu-jets, where the muons to which we applied the selection are nearly collinear. The mu-jet momentum minima are indicated with dashed lines in Fig. 2.

The trigger efficiency and offline muon reconstruction efficiency are derived as simple factors from  $Z \to \mu\mu$  data using a tag-and-probe technique.

## 2 Efficiency of near-by muons

#### 2.1 Trigger efficiency

128

129

For all signatures, we select events with the lowest unprescaled, unisolated, single-muon trigger available (see Appendix A for motivation). In the 2010A dataset (May-Aug 2010, 3 pb<sup>-1</sup>), this is HLT\_Mu9 and in the 2010B dataset (Sep-Oct 2010, 32 pb<sup>-1</sup>), this is HLT\_Mu15. Since the HLT\_Mu15 trigger does not exist in the 2010A data, we simulate it by requiring an L3 muon reconstructed with  $p_T > 15 \text{ GeV}/c$ . We also require at least one  $p_T > 15 \text{ GeV}/c$ ,  $|\eta| < 0.9$  muon offline, to be insensitive to the shape of trigger turn-on curves and nearby-muon inefficiencies in the endcap. The  $p_T$  resolution of L3 and offline muons are both dominated by tracker resolution.

The trigger response was studied in a generic way by simulating muon pairs with uniform mass, pair  $p_T$ , and pair  $\eta$  distributions (dimuon-gun MC). It is important to isolate dependencies of the efficiency on all physical variables in this unrealistic sample, as such a dependence would lead to model-dependent inefficiency in realistic cases.

In a dimuon-gun subsample with at least one  $p_T > 15 \text{ GeV/}c$  muon, the HLT\_Mu15 efficiency versus dimuon mass,  $\eta$ , and  $p_T$  are shown in Fig. 5. **FIXME:** Need to change all Mu11 plots to Mu15. The endcap region is inefficient for low-mass dimuons, and this inefficiency has a slight dependence on pair  $p_T$ .

To diagnose this further, we plot the efficiency as a function of how close the muon 146 trajectories approach each other in the muon system (Fig. 6). The closeness of the 147 muon trajectories is quantifed for  $0.9 < |\eta| < 2.1$  on a plane at |z| = 700 cm (ME1/2), 148 in terms of separation in azimuthal position  $\Delta \phi = \phi_{u^+} - \phi_{u^-}$  and and radial position 149  $\Delta r = r_{u^+} - r_{u^-}$ : the efficiency drops by a factor of two when  $|\Delta \phi| < 0.2$  and  $|\Delta r/z| < 0.2$ 0.2, though this efficiency loss is independent of leading muon  $p_T$ , as evidenced by the 151 turn-on curve within the spot. Dimuons of different mass/momentum combinations 152 sample this spot differently, as indicated by the labeled contour lines. Since the masses 153 and momentum distributions of new physics dimuons is unknown, the endcap trigger 154 efficiency cannot be quantified. That is why we require at least one above-threshold muon in the barrel per event. (This study was performed with a 2010B-like endcap 156 trigger simulation— no ME1/1 singles and modified ghost suppression— though the conclusion is the same for the 2010A-like endcap trigger simulation.) 158

FIXME: Need to update all HLT\_Mu11 plots to HLT\_Mu15 and simplify the presentation of this. In the exotica talk, we have a side-by-side comparison of efficiency vs.  $\eta$  for overlapping and non-overlapping trajectories: the difference is dramatic.

### 2.2 Reconstruction efficiency

### 2.3 Measurement of efficiency within acceptance cuts

**FIXME:** Reconstruction and trigger efficiency from *Z* tag-and-probe

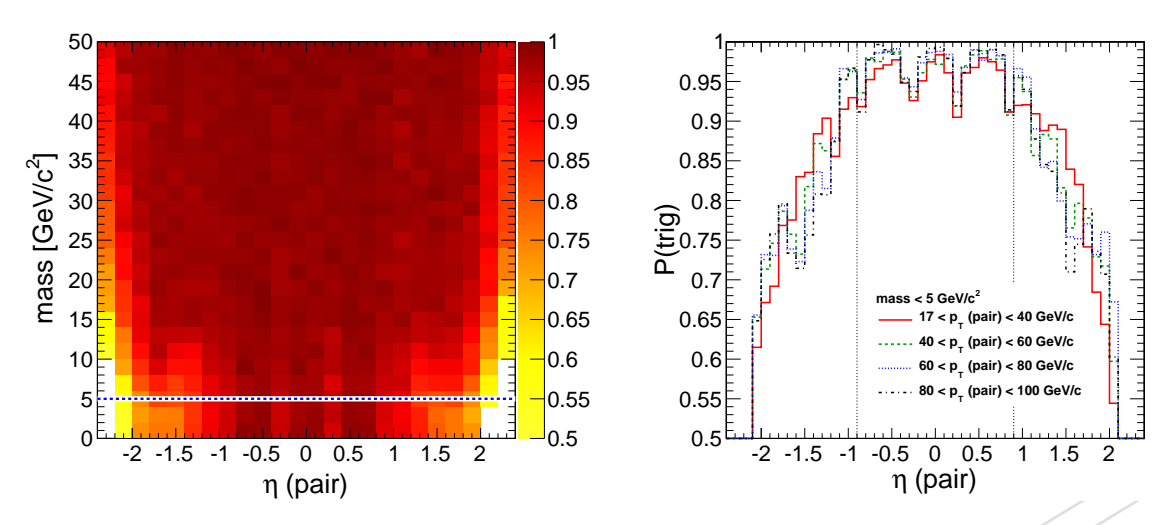


Figure 5: HLT\_Mu11 trigger efficiency as a function of mass, momentum, and pseudorapidity of dimuons in a dimuon-gun simulation. In both plots, trigger efficiency is the fraction of event passing the trigger in a sample with at least one  $p_T > 15 \text{ GeV}/c$  muon, the other unconstrained.

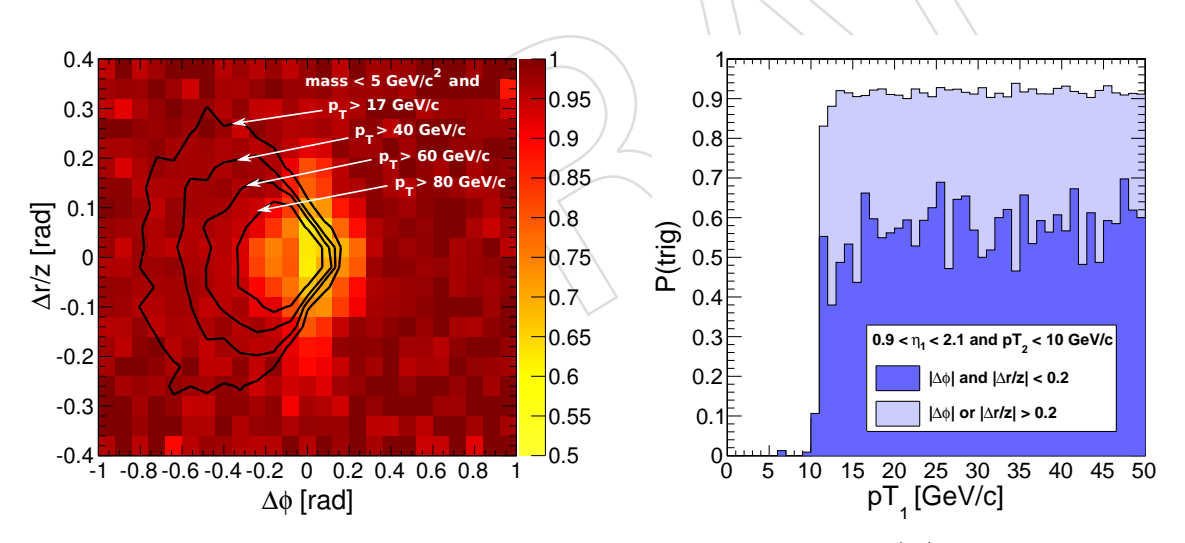


Figure 6: Diagnostic of HLT\_Mu11  $p_T$  dependence in  $0.9 < |\eta| < 2.1$ . Left: trigger efficiency (color scale) with one  $p_T > 15$  GeV/c muon, the other unconstrained, as a function of separation of muons in the muon system. Different mass/momentum combinations (the labeled contour lines) sample this spot to differing degrees. The trigger turn-on curve in the spot is unaffected; it is the plateau efficiency that is lowered.

# 3 Signal mass spectrum shape

Resonances coupling weakly to the Standard Model are by definition narrow, so their lineshapes are dominated by detector resolution and final state radiation of a photon from one of the muons. The Standard Model provides four resonances in our mass range of interest,  $\omega$ ,  $\phi$ ,  $J/\psi$ , and  $\psi'$ , which we use to calibrate the signal lineshapes. These resonances are typically produced with low momentum, so we additionally simulate low and high momentum resonances with a dimuon-gun Monte Carlo.

The most general lineshape used in this study is a first-order Crystal Ball double-Gaussian with a linear background. None of the resolution studies use all of the features of this curve in a single fit, but each feature is used in some study. An expression for the curve as f(m) with m as invariant mass (in  $\text{GeV}/c^2$ ) is

$$S(m; m_0, \sigma, \alpha, f_{0.07}, p_0, p_1) = p \left[ (1 - f_{0.07}) CB(m; m_0, \sigma, \alpha) + f_{0.07} G_{0.07}(m; m_0) + p_0 + p_1 m \right]$$
(1)

where

$$CB(m; m_0, \sigma, \alpha) = \begin{cases} \frac{1}{\sqrt{2\pi}\sigma} \exp\left(-(m - m_0)^2/(2\sigma^2)\right) & \text{if } (m - m_0)/\sigma > -\alpha\\ \frac{2}{5\sigma} \exp\left(-\alpha^2/2\right)/(1 - \alpha^2 - (m - m_0)/\sigma) & \text{otherwise} \end{cases}$$
(2)

and

$$G_{0.07}(m; m_0) = \frac{1}{\sqrt{2\pi} \, 0.07} \exp\left(-(m - m_0)^2 / (2 \cdot 0.07^2)\right) + p_0 + p_1 m\right]. \tag{3}$$

The peak of the mass distribution (true mass of the particle in this parameterization) is  $m_0$  (GeV/ $c^2$ ), with core resolution  $\sigma$  (GeV/ $c^2$ ). The Crystal Ball parameter  $\alpha$  indicates where the core Gaussian smoothly connects to a low-side  $1/(m-m_0)$  tail (in number of standard deviations below the peak). A second, 0.07 GeV/ $c^2$  wide Gaussian is scaled by  $f_{0.07}$ ; for most observed distributions,  $f_{0.07} \rightarrow 0$ . The linear background is  $p_0 + p_1 m$ .

Fits to the Standard Model resonances are shown in Fig. 7. The data are required to contain exactly two muons with vector-sum  $p_T < 80 \text{ GeV/}c$ , where at least one has  $p_T > 15 \text{ GeV/}c$  and  $|\eta| < 0.9$ . The masses are all fixed to PDG values. In the  $\omega$  fit, the  $\rho$  is included with an intrinsic width fixed to its PDG value and allowed to float in normalization, as an additional background. In all resonance-fits, the double-Gaussian was suppressed ( $f_{0.07}$  fixed at zero), since the double-Gaussian behavior is observed only in the endcap. Only in the  $J/\psi$  fit is the Crystal Ball tail allowed to float: the fitted value,  $\alpha = 2.04 \pm 0.11$ , is fixed in the other three resonance fits. **FIXME:** Should say something about the poor  $J/\psi$  fit or make it better, not that it matters for the analysis.

To quantify the resolution of dimuons over the whole  $\eta$  range, we used a dataset with three muons: two belong to the same mu-jet and the third is used to satisfy the trigger

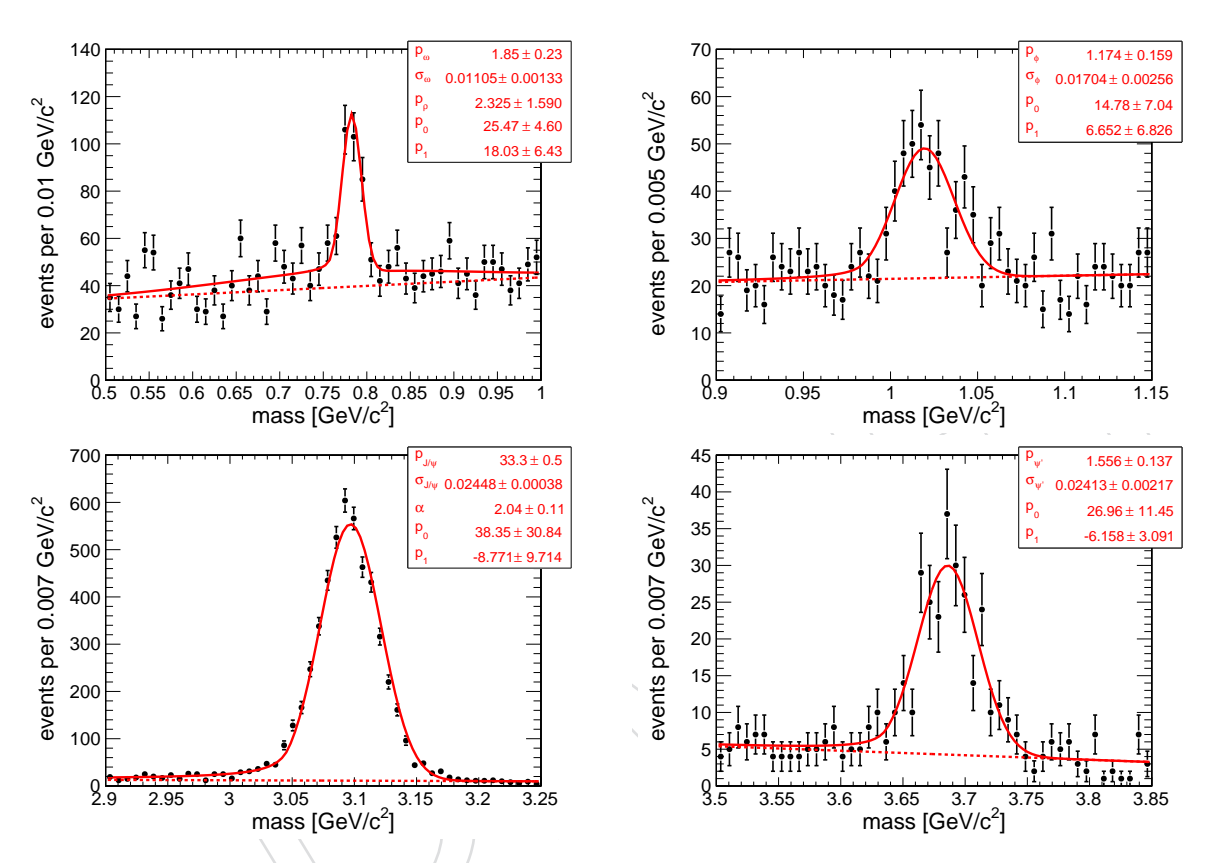


Figure 7: Four resonance mass peak fits in dimuon data:  $\omega$  (top-left),  $\phi$  (top-right),  $J/\psi$  (bottom-left), and  $\psi'$  (bottom-right). All masses are fixed to PDG values; see text for a complete list of fixed/free parameters.

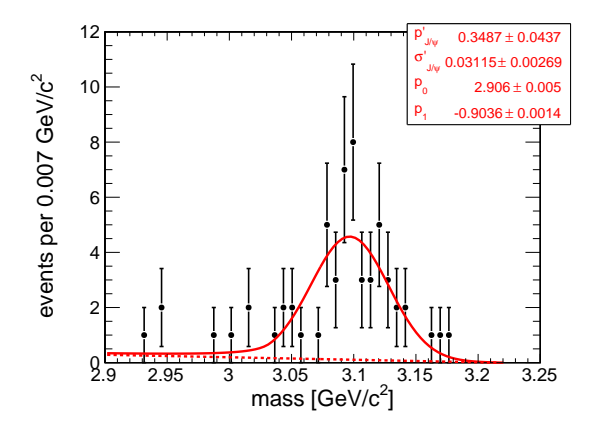
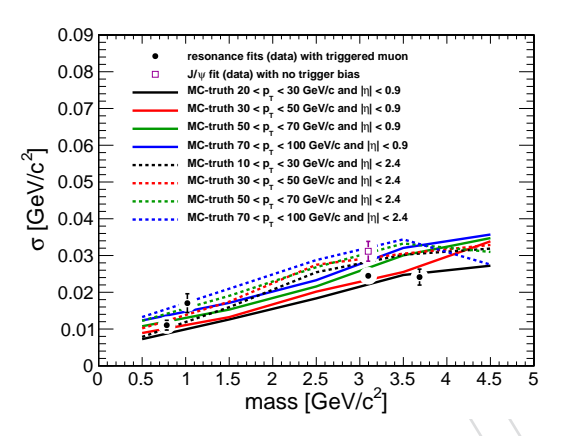


Figure 8:  $J/\psi$  fit in dimuon-plus-muon data, where the third muon is used to satisfy the trigger. The  $\sigma$  observed in this fit applies to the full  $\eta$  range, not just the barrel.



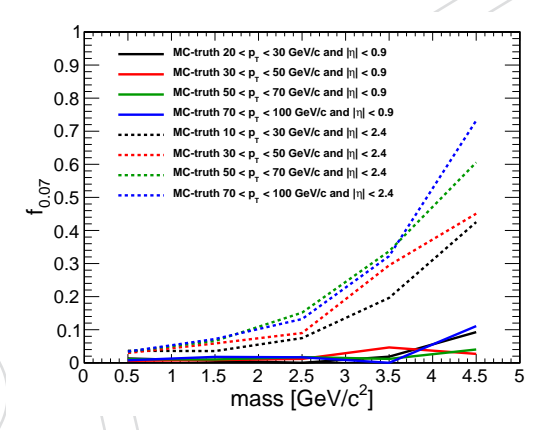


Figure 9: Left: resolution as a function of mass for simulated muons (lines) and real resonances (points). Right: the double-Gaussian parameter  $f_{0.07}$  for simulated muons.

( $p_T > 15$  GeV/c,  $|\eta| < 09$ , matched to a trigger-level muon). Since these events are much more rare than dimuons, we only fit the  $J/\psi$ , and fix  $\alpha$  to the value quoted above and  $f_{0.07}$  to zero. The fitted peak is presented in Fig. 8.

For more sensitivity to extremes in  $p_T$  and  $\eta$ , distributions of reconstructed mass minus generator-level mass from the dimuon gun Monte Carlo were fitted to double Gaussians. Backgrounds ( $p_0$  and  $p_1$ ) and final-state radiation ( $\alpha$ ) were not included in the fit because the effects were not simulated. Figure 9 summarizes the results of these fits in bins of dimuon  $p_T$ , mass, and  $\eta$  coverage. The results of the resonance data fits are overlaid for comparison. The core Gaussian dependence on  $p_T$  and  $\eta$  are weak, but higher momenta and larger  $\eta$  coverage yield slightly wider core resolutions. The double-Gaussian part of the distribution, however, grows strongly as a function of mass for high- $p_T$  dimuons in the endcap.

## 4 Background mass spectrum shape

### 4.1 Study of low-mass dimuon spectrum

The shape templates for background mass distributions are derived from background-enriched samples, in which the Standard Model backgrounds dominate over any potential signals. The background-enriched samples are chosen to have the same physics content as in the signal regions, which requires a thorough understanding of the background data. As a first step, we investigate the  $0.25–5~{\rm GeV}/c^2$  single-dimuon spectrum with vector-sum  $p_T < 80~{\rm GeV}/c$ . Figure 10 shows a "raw" mass spectrum, with only the following cuts:

- at least one  $p_T > 15 \text{ GeV}/c$ ,  $|\eta| < 0.9 \text{ muon}$ ;
- exactly one additional muon, with  $p_T > 5 \text{ GeV}/c$  and  $|\eta| < 2.4$ ;
- at least one  $p_T > 15 \text{ GeV}/c \text{ L3 muon}$ , to emulate the HLT\_Mu15 trigger.

The data are overlaid by Monte Carlo distributions, all scaled to the integrated luminosity of the dataset (35 pb $^{-1}$ ). The following Monte Carlo samples were used:

- Drell-Yan, generated by Pythia 8 to avoid an internal mass cut in Pythia 6 (with pile-up);
- prompt  $J/\psi \to \mu\mu$ ,  $\psi' \to \mu\mu$ , and  $\psi' \to J/\psi \pi\pi \to \mu\mu \pi\pi$ , produced with Pythia 6, decayed with EvtGen, including Photos for final state radiation;
- inclusive-muons from QCD with  $\hat{p}_T > 30 \, \text{GeV}/c$ , generated by Pythia 6 and divided into three partitions:
  - bb with one b-quark decaying to μμX by double-semileptonic decay or dimuon resonances (both muons have the same B hadron as a common ancestor in the generator-level decay tree);
  - muons from light-flavor hadronization and muons that are unassociated with one another, excluding fakes and decays-in-flight;
  - at least one fake muon and/or decay-in-flight of a charged pion, charged kaon, or strange baryon.

The two most useful tools for analyzing the physics content of the distribution are isolation and flight distance. We define track-based isolation by

Iso = 
$$\sum_{\text{tracks}} p_T$$
 if  $p_T > 1.5 \text{ GeV}/c$ ,  $\Delta R < 0.4$ , and not a muon, (4)

such that the two close-by muons do not veto one another. The  $p_T$  threshold and  $\Delta R$  radius were optimized for insensitivity to pile-up and for a flat distribution near Iso = 0 in  $b\bar{b}$  Monte Carlo. Distributions of Iso for the whole mass distribution, "continuum" (1.1 < mass < 2.9 GeV/ $c^2$ ), and "low-mass" (0.35 < mass < 0.5 GeV/ $c^2$ ) regions are given in Fig. 11. (The continuum and low-mass cuts are indicated by dotted vertical lines in Fig. 10.) As expected, Drell-Yan and prompt resonances are well isolated, while

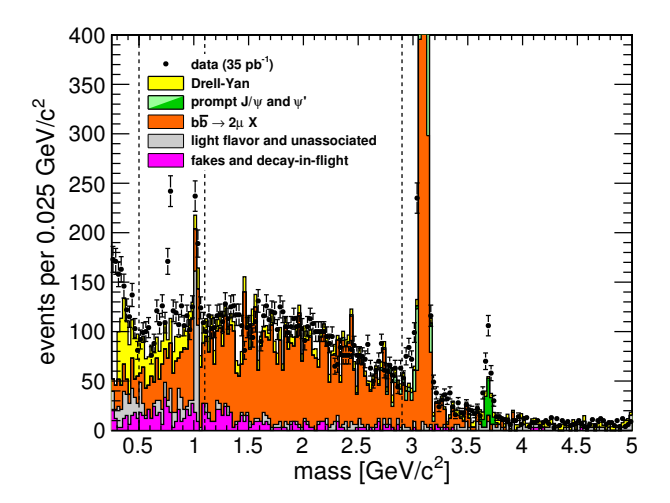


Figure 10: Mass distribution of single-dimuon events with Monte Carlo simulations superimposed. (See text for details about the cuts and the Monte Carlo samples.)

 $b\bar{b}$  is not.

234

237

239

240

242

245

246

The flight distance is defined as

$$L_{xy} = \frac{(v_x - V_x)p_x + (v_y - V_y)p_y}{\sqrt{p_x^2 + p_y^2}}$$
 (5)

where  $(v_x, v_y)$  is the 2-D position of the dimuon vertex,  $(p_x, p_y)$  is the 2-D projection of the dimuon momentum vector, and  $(V_x, V_y)$  is the 2-D position of the closest primary vertex in the z direction (z is parallel with the beamline). Figure 12 shows distributions of  $L_{xy}$  in the same mass bins as isolation. Vertices with negative  $L_{xy}$  are mis-measured; this provides a direct indication of the vertex resolution. Drell-Yan and prompt resonances form a peak centered on  $L_{xy} = 0$ , while  $b\bar{b}$  has a long tail toward positive  $L_{xy}$  due to the long lifetimes of B hadrons. Vertex resolution degrades when the opening angle is small, which is why the symmetric peak in the low-mass bin is wider than in all other bins.

From *Iso* an  $L_{xy}$ , we can see that the two major components of the data are  $b\bar{b}$  and prompt/Drell-Yan, each containing resonance and continuum contributions. We can partition the sample using the following " $b\bar{b}$  cuts,"

$$Iso > 4.5 \text{ GeV/}c \text{ or } L_{xy} > 2 \text{ mm.}$$
 (6)

These threshold are indicated with dotted vertical lines in Figs. 11 and 12. The invariant mass distribution with  $b\bar{b}$  and anti- $b\bar{b}$  cuts is shown in Fig. 13. The inclusive-muon sample is missing  $\omega$  and  $\psi'$  resonances, while the prompt/Drell-Yan is missing only the  $\omega$ . Most of the dimuons arising from fakes and decays-in-flight pass the  $b\bar{b}$  cut, comprising about 25% of the events passing the cut below 1 GeV/ $c^2$ . Below 0.5 GeV/ $c^2$ ,

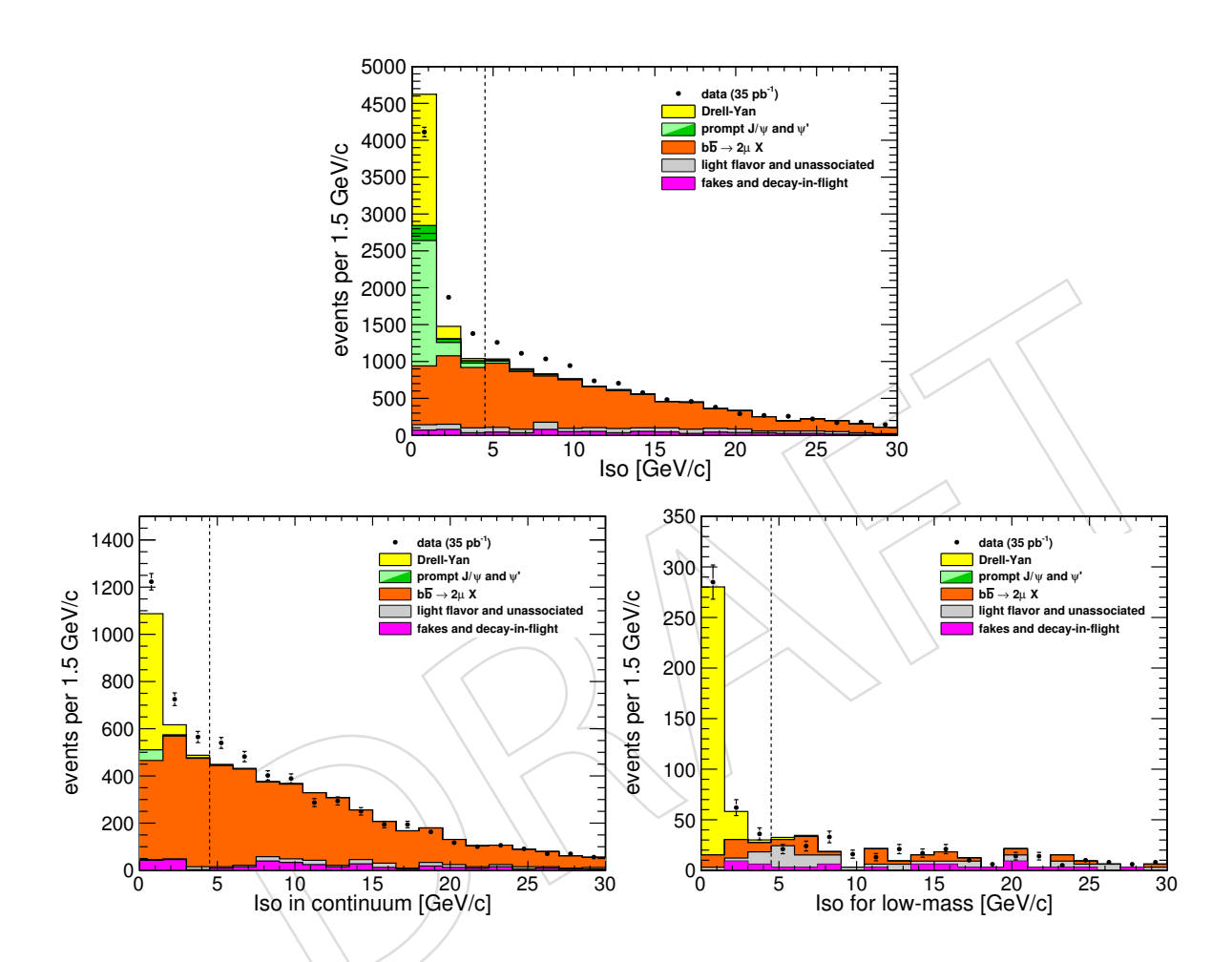


Figure 11: Track-based isolation (see text for definition) for the whole sample (top),  $1.1-2.9 \, \text{GeV}/c^2$  continuum (bottom-left), and  $0.35-0.5 \, \text{GeV}/c^2$  low-mass region (right).

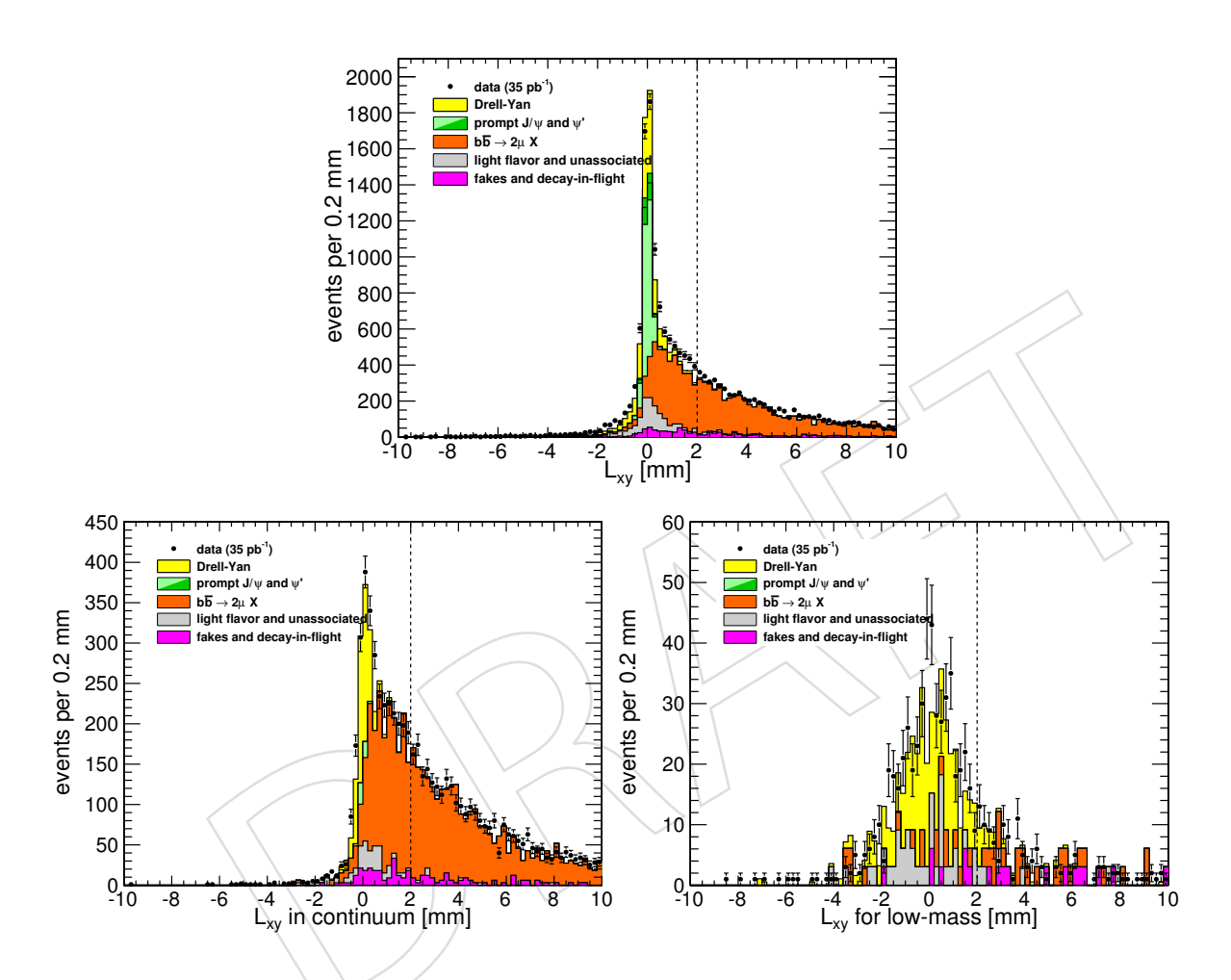


Figure 12: Distance of the dimuon vertex (in x-y) from the closest primary vertex (in z), along the direction of the dimuon momentum axis, for the whole sample (top), 1.1–2.9 GeV/ $c^2$  continuum (bottom-left), and 0.35–0.5 GeV/ $c^2$  low-mass region (right).

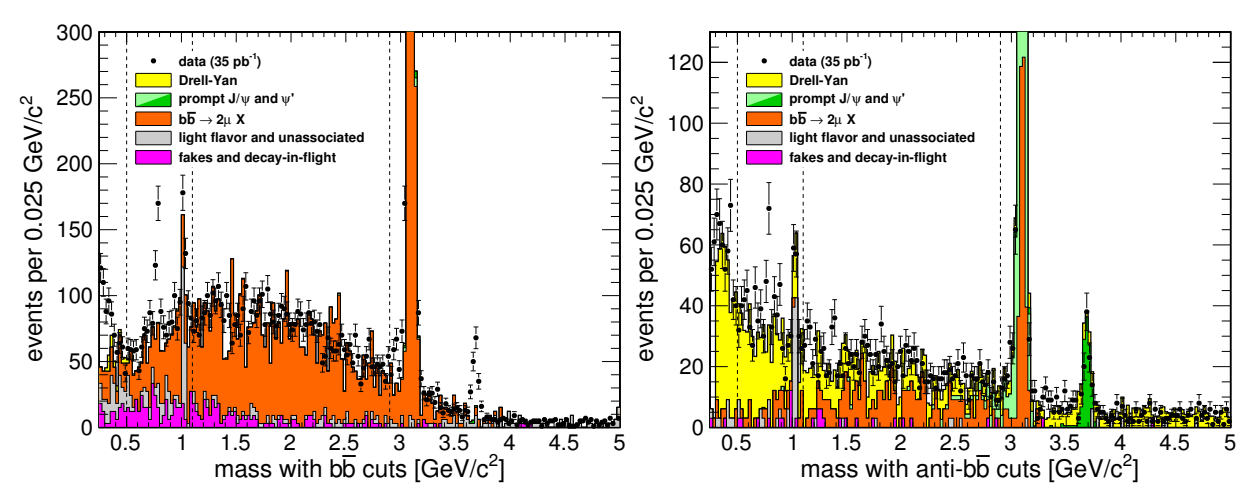


Figure 13: The mass distribution partitioned by  $b\bar{b}$  cuts.

there is a low-mass rise not described by the Monte Carlo, and this distribution is to wide to be a detector resolution-dominated  $\mu\mu$  resonance.

The low-mass rise has an endpoint near the  $\eta$  mass (0.55 GeV/ $c^2$ ), and  $\eta$  has a large branching fraction to  $\mu\mu\gamma$  (3 × 10<sup>-4</sup>, which is comparable to branching fractions for  $\omega \to \mu\mu$  and  $\phi \to \mu\mu$ ), which is much larger than its branching fraction to  $\mu\mu$  (6 × 10<sup>-6</sup>). We therefore consider that the low-mass rise might be  $\eta \to \mu\mu\gamma$  events reconstructed without the photon, and attempt to find the photon. Figure 14 shows a  $\mu\mu\gamma$  invariant mass and a close-up of the  $\mu\mu$  invariant mass, both with  $b\bar{b}$  cuts. The photons are reconstructed using the particle-flow photon algorithm, and exactly one is required within  $\Delta R < 0.1$  of the dimuon axis. A significant  $\eta$  peak containing 63±15  $\eta \to \mu\mu\gamma$  events is observed in  $\mu\mu\gamma$ , compared to about 170 in the  $\mu\mu$  low-mass rise. **FIXME:** Need to know the efficiency of finding  $\mu\mu\gamma$  with this technique compared to the efficiency of finding  $\mu\mu$ . It is important that the photon-finding efficiency is evaluated *in jets.* At least 1/3 of the low-mass rise is due to the  $\eta$  resonance.

### 4.2 Mass template for (a-1): high- $p_T$ dimuons

The (a-1) signal region, exactly one dimuon with vector-sum  $p_T > 80 \text{ GeV}/c$ , has a mass template derived from low-momentum dimuons. For a background-enriched sample, we use dimuons with  $40 < p_T < 60 \text{ GeV}/c$ , and then test it in a  $60 < p_T < 80 \text{ GeV}/c$  control sample. The control sample is also background-dominated for  $\lesssim 1 \text{ pb}$  signals, but it is closer in kinematics to the signal region.

The choice of 40–60 and 60–80 GeV/c regions is motivated by the fact that the major components of the data scale proportionally with  $p_T$  above 40 GeV/c. Figure 15 shows the  $p_T$  distribution of the data partitioned into three classes:

- non- $J/\psi$  events passing the  $b\bar{b}$  cuts;
- $J/\psi$  events passing the  $b\bar{b}$  cuts;

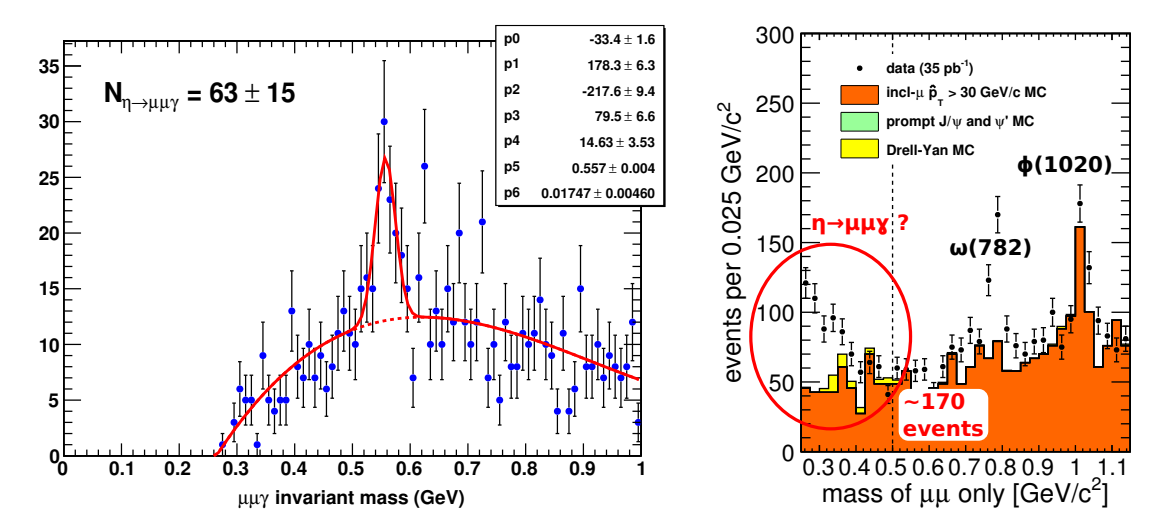


Figure 14: Left: three-body  $\mu\mu\gamma$  mass distribution, in which exactly one particle-flow photon is required within  $\Delta R < 0.1$  of the dimuon axis. Right: a close-up of the low-mass excess in  $\mu\mu$  with the same cuts.

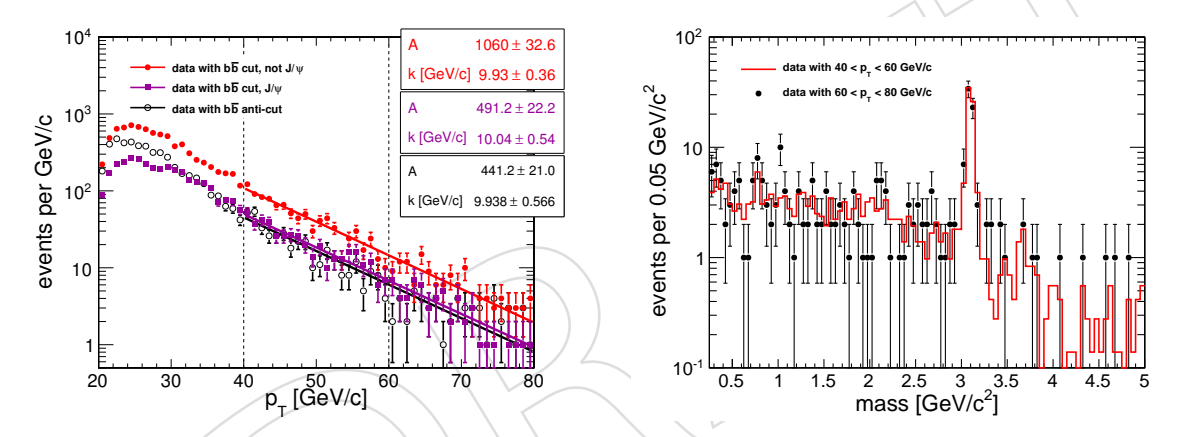


Figure 15: Scaling of single-dimuon data with  $p_T$ . Left:  $p_T$  spectra for three non-overlapping subsamples of dimuons ( $\propto \exp(-x/k)$ , normalized by A, the integral from 40 to 80 GeV/c). Right: mass spectrum in two bins of  $p_T$ , scaled to equal area.

### • events failing the $b\bar{b}$ cuts;

275

277

279

280

where  $J/\psi$  events are selected with a  $0.15~{\rm GeV/c^2}$ -wide mass window around the PDG  $J/\psi$  mass. Each of these three distributions is exponential with mutually consistent length scales:  $k=9.93\pm0.36$ ,  $10.04\pm0.54$ , and  $9.94\pm0.57$  for the three classes respectively when fitted to  $A\exp(-x/k)$ . In the accompanying figure, the shape of the 40– $60~{\rm GeV/}c$  mass distribution (without  $b\bar{b}$  cuts) is overlaid on the 60– $80~{\rm GeV/}c$  mass distribution, and they appear to be consistent. To verify that this consistency in shape continues into the signal region, we plot inclusive-muon Monte Carlo mass distributions in  $20~{\rm GeV/}c$  bins of  $p_T$  from  $40~{\rm to}~120~{\rm GeV/}c$ .

The template shape for the (a-1) region is obtained by fitting the 40-60 GeV/c mass

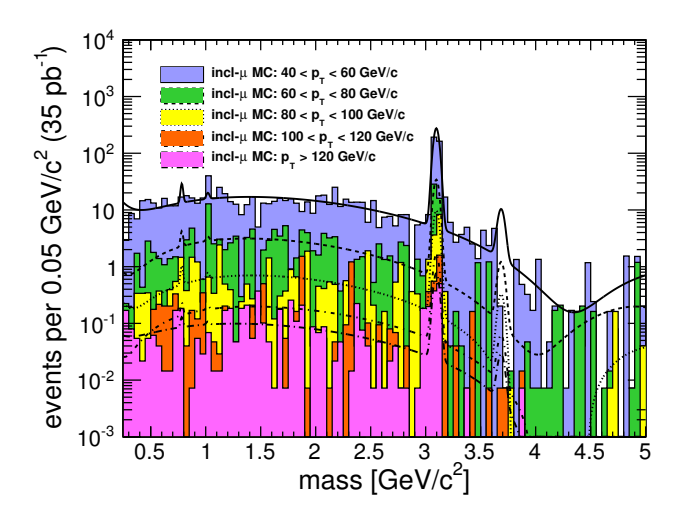


Figure 16: Mass distribution of inclusive-muon MC in bins of  $p_T$  from 40 to 120 GeV/c.

distribution to the following curve:

$$B(m; p_R, f_{\omega}, f_{\phi}, f_{\psi}, f_m, p_{-1}, p_0, p_1, p_2, p_3, p_4) = p_R \left[ f_{\omega} G(m; 0.78265, 0.011) + f_{\phi} G(m; 1.019455, 0.014) + G(m; 3.096916, 0.025) + f_{\psi'} G(m; 3.68609, 0.029) + \frac{f_m}{m} \right] + \frac{p_{-1}}{m} + p_0 + p_1(m - 5) + p_2(m - 5)^2 + p_3(m - 5)^3 + p_4(m - 5)^4.$$
 (7)

The  $p_R$  parameter normalizes all resonances, with  $f_\omega$ ,  $f_\phi$ ,  $f_{\psi'}$ , and  $f_m$  normalizing the individual resonances with respect to the  $J/\psi$ . The function  $G(m;m_0,\sigma)$  is a Gaussian with  $m_0$  (centroid) and  $\sigma$  (resolution) in GeV/ $c^2$ . For each resonance,  $m_0$  is fixed to its PDG mass and  $\sigma$  is fixed to the resolution obtained in Sec. 3. The  $f_m$  term describes the low-mass rise, categorized here as a resonance because of its large  $\eta \to \mu \mu \gamma$  component. The  $p_{-1}$ ,  $p_0$ ,  $p_1$ ,  $p_2$ ,  $p_3$ ,  $p_4$  terms are an expansion of the background shape as a Taylor/Laurent polynomal. For the (a-1) region,  $p_{-1}$  is fixed to zero. Figure 17 shows a fit of the background-enriched data to this shape, and an overlay of the shape on the control region.

### 4.3 Mass template for (a-2) and (a-3): high-multiplicity mu-jets

The (a-2) signal region consists of exactly one neutral mu-jet with four muons, and the (a-3) region is exactly one mu-jet with more than four muons. Standard Model processes that yield these topologies with real muons are rare (primarily boosted  $b\bar{b}$ ), so the dominant backgrounds are mu-jets containing fake and decay-in-flight muons. "Fake" muons are rare failures of the muon identification procedure, in which muon chamber segments from one real muon are assigned to two distinct tracks in the tracker.

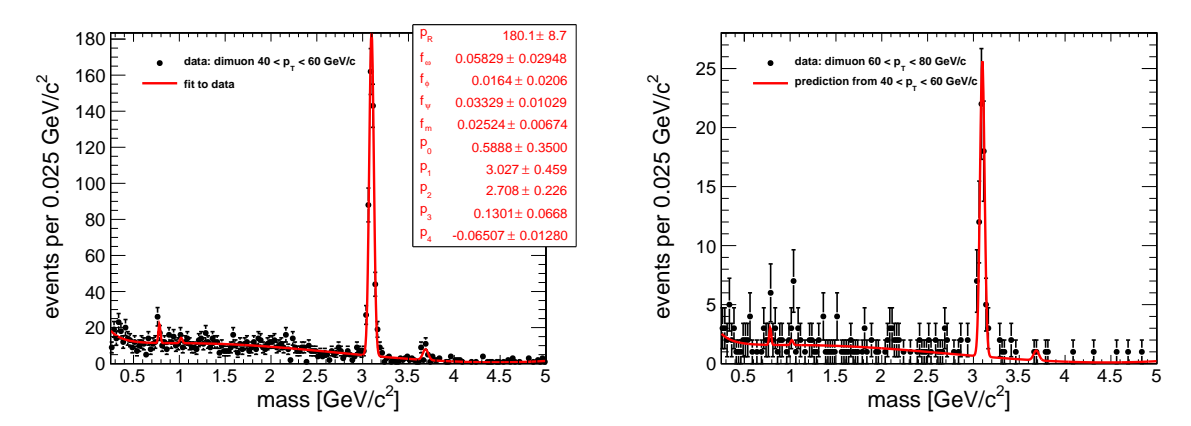


Figure 17: Left: fit of the (a-1) background-enriched data to Eqn. 7. Right: overlay of the same shape on the corresponding control region.

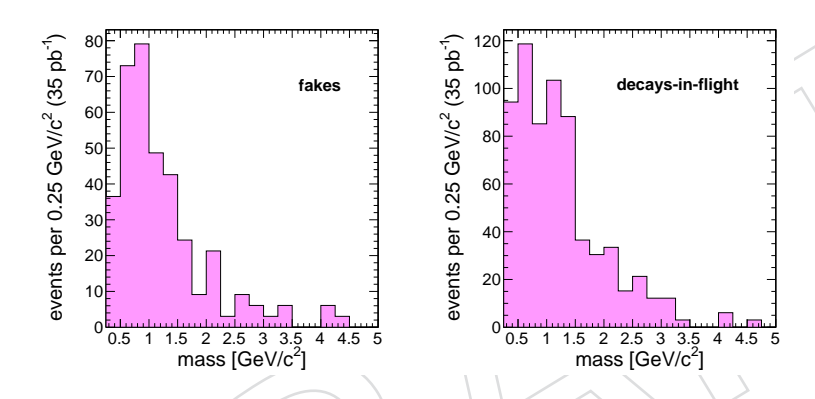


Figure 18: Distributions of dimuon mass for dimuons containing fake and decay-in-flight muons in inclusive-muon Monte Carlo.

Decays-in-flight are  $\pi^{\pm} \to \mu^{\pm} \nu$ ,  $K^{\pm} \to \mu^{\pm} \nu$ , and (less frequently) strange baryons producing a muon far from the primary and secondary vertices. Dimuons containing a fake or a decay-in-flight muon typically have low mass distributions, peaking at  $1 \text{ GeV}/c^2$  as shown in Fig. 18. The distributions are similar because in both cases, a real muon is paired with a random hadronic particle.

The shape of the dimuon mass distribution with a fake or decay-in-flight muon can be quantified using data by pairing real muons with random hadronic tracks. We search for tracks near mu-jets with the same properties as quality TrackerMuons, except that no requirement is made on the muon chamber segments. We require the track to satisfy:

- $p_T > 5 \text{ GeV}/c \text{ and } |\eta| < 2.4$ ;
- number of hits  $\geq 8$ ;
- $\chi^2/N_{\rm DOF} < 4$ ;

298

299

300

301

302

303

305

307

308

309

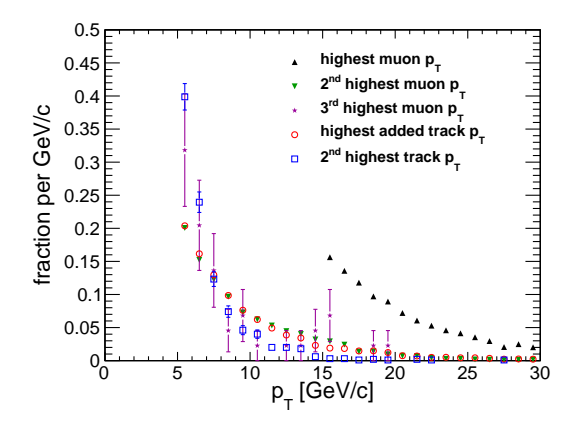


Figure 19: Momentum distributions of muons and extra tracks in a sample where random tracks have been added to mu-jets. Only the highest- $p_T$  muon is biased (by the trigger requirement).

and the track at at least one muon in the mu-jet must satisfy:

• opposite charge;

312

313

314

315

316

317

318

319

320

321

322

323

- invariant mass  $< 5 \text{ GeV}/c^2$ ;
- vertex probability > 1%;
- $\Delta R$  < 0.01 if either of the above fail (including vertex reconstruction).

Thus, the extra track or tracks have the same distributions as muons in a mu-jet, with the exception of muon chamber segments. Figure 19 shows the  $p_T$  distributions of muons and extra tracks in these samples.

The background-enriched sample is the set of dimuons with two extra tracks and zero net charge, and the control sample is the set of three-muon mu-jets with one extra track and zero net charge. Figure 20 shows a fit to the background-enriched sample and its overlay on the control sample. The fit ansatz is Eqn. 7 with  $f_{\omega}$ ,  $f_{\phi}$ ,  $f_{\psi'}$ , and  $f_m$  fixed to the values obtained in Fig. 17 (resonances are dwarfed by continuum shape). To demonstrate the universality of the fake dimuon shape, the Monte Carlo distribution of fakes and decays-in-flight in dimuons is overlaid.

As an additional control region, closer to the signal, we show the 2-D mass distribution of fundamental dimuon masses in four-muon mu-jet events (Fig. 21). The signal region along the diagonal is blinded by a strip that is 5- $\sigma$  wide in detector resolution, to hide a potential discovery before finalizing the procedure. Only one event is observed in the off-diagonal region, consistent with a simple back-of-the-envelope scaling: the ratios of two muons plus two extra tracks ( $N_{2+2}$ ), three muons plus one extra track ( $N_{3+1}$ ), and four muons with no extra tracks ( $N_{4+0}$ ) are as follows:

$$\frac{N_{3+1}}{N_{2+2}} = 0.014 \text{ and } \frac{N_{4+0}}{N_{3+1}} = 0.03.$$
 (8)

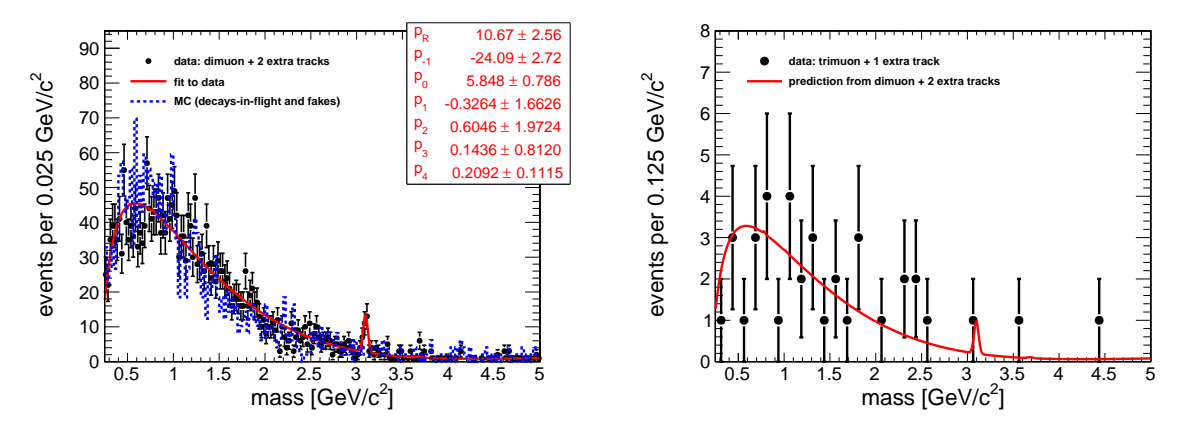


Figure 20: Left: fundamental dimuon distribution from neutral two muon plus two extra track mu-jets. Right: same for neutral three muon plus one extra track mu-jets. Blue distribution is fake and decay-in-flight dimuons in Monte Carlo.

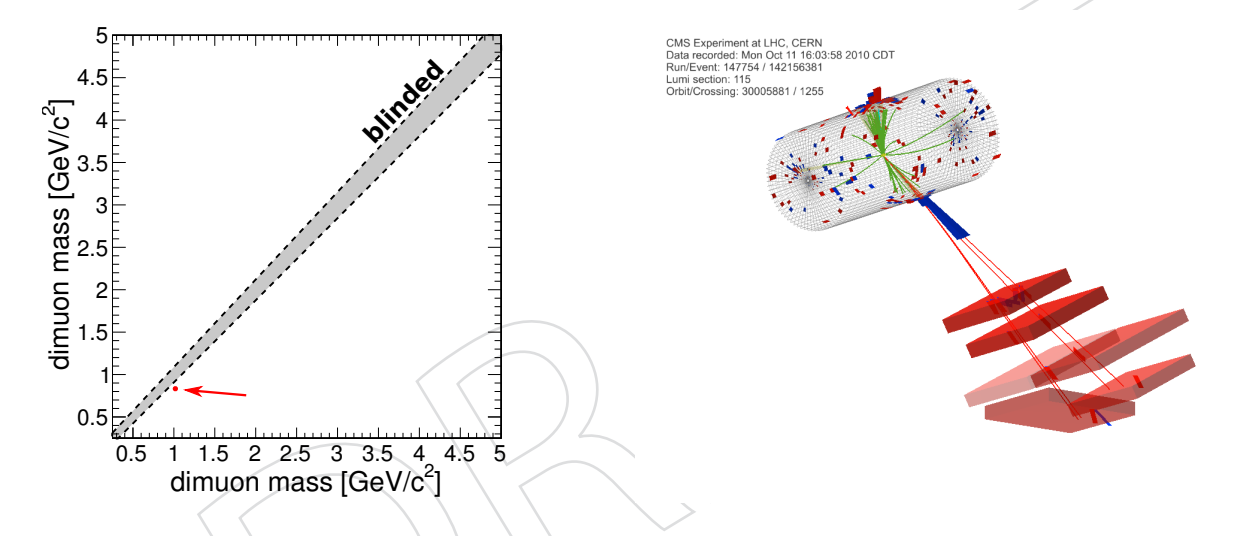


Figure 21: Left: fundamental dimuon-dimuon mass plane for signal region (a-2) with the strip along the diagonal blinded (5- $\sigma$  in detector resolution). Right: a display of the single event surviving cuts.

The single observed event has fundamental dimuon masses of 0.8 and 1.0 GeV/ $c^2$ , in the bulk of the predicted distribution (Fig. 20). Three of its four muons have only two segments each, though their trajectories all pass through four stations. The pattern of segments suggest only two real muons.

### 4.4 Mass template for (b-1): events with two dimuons

327

328

329

330

The (b-1) signal region consists of events with two dimuons, a signature that is predominantly produced in the Standard Model by  $b\bar{b}$  with both b-quarks decaying to  $\mu\mu X$ . As such, the background-enriched samples should be  $b\bar{b}$ . The  $b\bar{b}$  cuts defined in

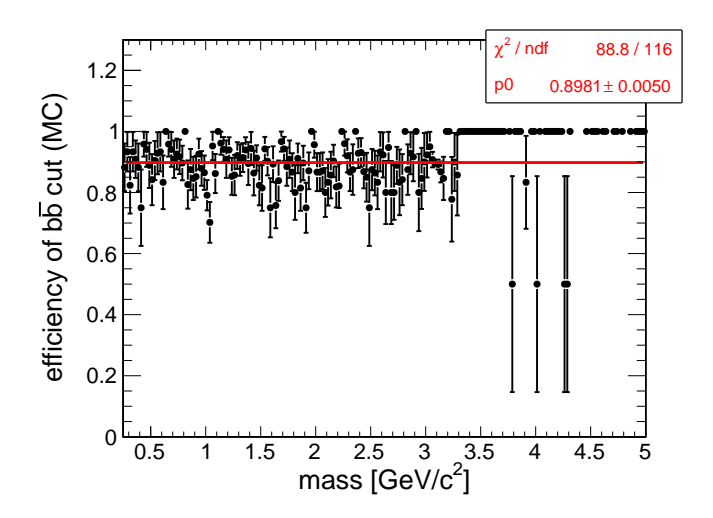


Figure 22: Efficiency of the  $b\bar{b}$  cut for simulated  $b\bar{b}$  events, demonstrating that the efficiency is constant, so the  $b\bar{b}$  cuts do not introduce a shape bias.

Eqn. 6 yield a nearly pure sample of  $b\bar{b}\to\mu\mu X$  when applied to dimuons (Fig. 13). In Fig. 22, we show that they also do not distort the  $b\bar{b}$  dimuon mass distribution, so we use this distribution as a background-enriched template.

Only one of the two dimuons in the (b-1) signal region needs to contain a muon satisfying the trigger, which implies a minimum  $p_T$  of  $20~{\rm GeV}/c$  and a direction that points into the barrel of the muon system ( $|\eta| \lesssim 0.9$ ). Since the other dimuon does not need to satisfy the trigger, its minimum  $p_T$  is  $10~{\rm GeV}/c$  and it can point anywhere in the muon system ( $|\eta| \lesssim 2.4$ ). The difference in  $p_T$  threshold modifies the mass spectrum, so the "other dimuon" mass template must be derived from a background-enriched sample without biasing the dimuon kinematics with the trigger. To do this, we use events with one dimuon and one extra muon. The third muon is required to satisfy the trigger, freeing the dimuon from this constraint. Three-muon events with a small angle between two of the muons are predominantly  $b\bar{b}$  with one b-quark decaying to  $\mu\mu X$  and the other to  $\mu X$ .

The asymmetry between triggered dimuon and other dimuon introduces another complication: in some double-dimuon events, both dimuons satisfy the trigger. In such cases, we assign the "triggered dimuon" and the "other dimuon" labels randomly. This does not bias the triggered dimuon distribution, but the part of the other dimuon phase space that would satisfy the trigger is depleted by a factor of two. We want the mass templates to reflect this, so we apply the same bias to the corresponding background-enriched sample. In the dimuon plus third muon sample, we weight events in which the dimuon could have triggered the event by a factor of 1/2. Figure 23 shows the results of a toy Monte Carlo demonstrating this effect.

Fits to both background-enriched samples are presented in Fig. 24. The dimuons with

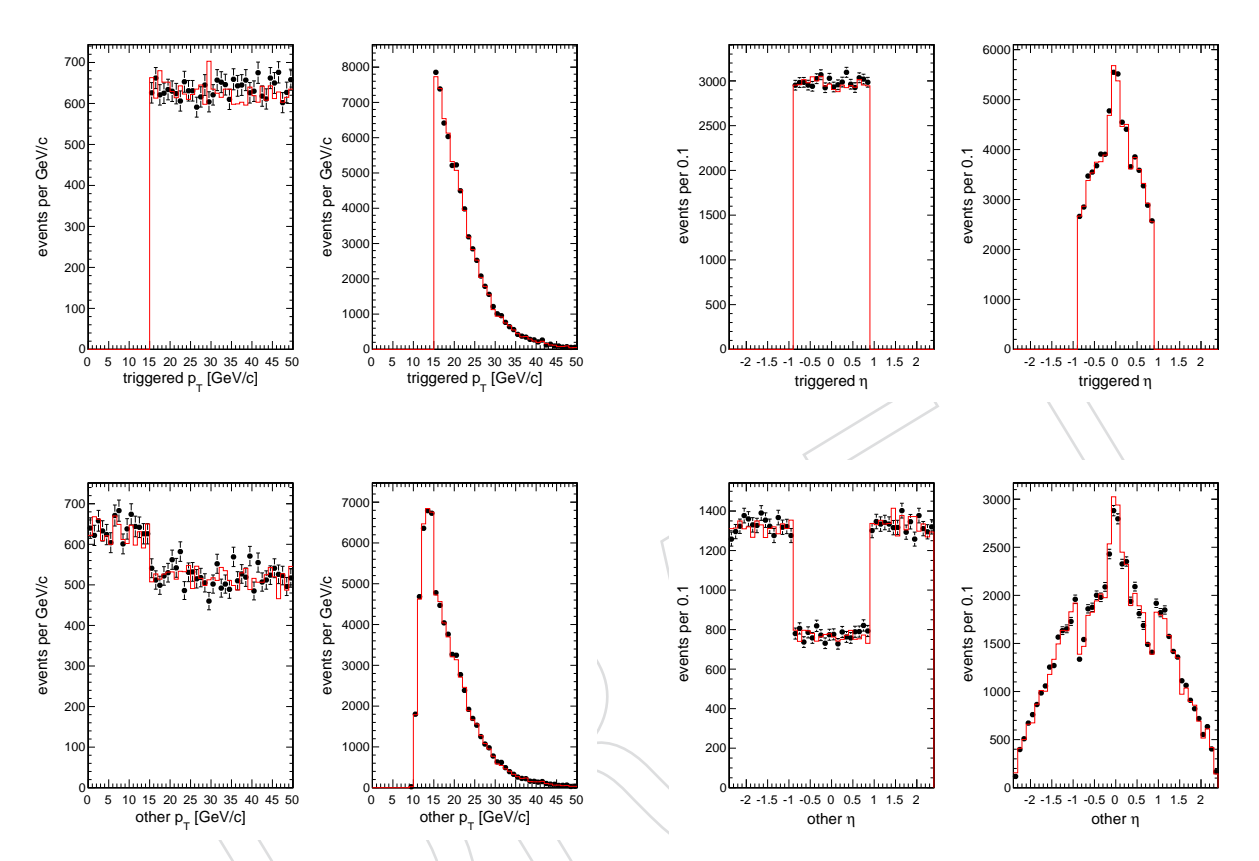


Figure 23: Toy Monte Carlo simulation of backgrounds in the dimuon-dimuon sample (black points), extrapolated from single-dimuons and dimuon-plus-muon background-enriched samples (red lines). In each pair of plots, the left is a simplified model with uniform  $p_T$  and  $\eta$  distributions and the right is a model with realistic  $p_T$  and  $\eta$  distributions. The "other dimuon" distribution is depleted in the signal region, but the background-enriched sample is weighted to have the same distribution.

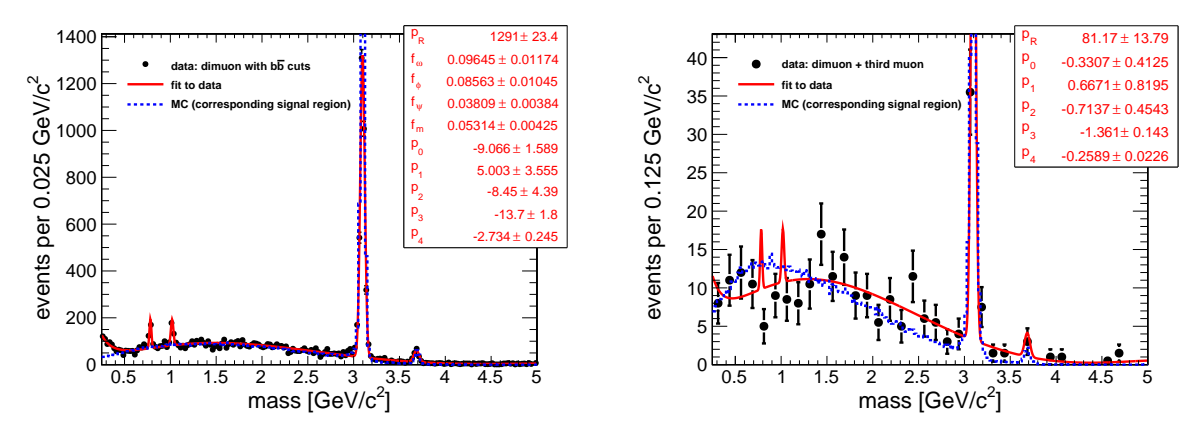


Figure 24: Left: dimuons with  $b\bar{b}$  cuts (background-enriched region for triggered dimuon). Right: dimuons plus extra muon (background-enriched region for other dimuon). Both are overlaid by template shape fits and Monte Carlo samples for the corresponding signal region.

 $b\bar{b}$  cuts sample (for triggered dimuons) is fitted to Eqn 7 with only  $p_{-1}$  fixed to zero, and the low-statistics dimuons plus third muon sample (for other dimuons) is fitted to the same ansatz with  $f_{\omega}$ ,  $f_{\phi}$ ,  $f_{\psi'}$ , and  $f_m$  fixed to the values determined by the first fit. Monte Carlo distributions for the corresponding  $b\bar{b} \rightarrow 2\mu 2\mu X$  signal region are overlaid to show the difference between the data-driven template shape and a template shape that could have been derived from Monte Carlo.

The control region for (b-1) is the off-diagonal part of the dimuon-dimuon mass plane. Figure 25 shows this plane with a 5- $\sigma$  strip along the diagonal blinded. Only ten events were observed, which is consistent with back-of-the-envelope scaling of the  $b\bar{b} \to 2\mu X$  sample: 12 841 events times 0.2%  $\mathcal{B}(b \to 2\mu X)$  (EvtGen) = 25 events. The distribution of these events appears to be consistent with the shapes of the background-enriched samples and inconsistent with fake or decay-in-flight distributions (Fig. 20).

The 2-D background shape template is built from a Cartesian product of the triggered dimuon shape and the other dimuon shape. To demonstrate that this is valid, a large Monte Carlo sample of  $b\bar{b} \rightarrow 2\mu \, 2\mu \, X$  was generated using Pythia 6 and EvtGen. Figure 26 shows the rectilinear structure of the simulated dimuon-dimuon mass plane and projections of the whole plane overlaid on slices around the  $J/\psi$  resonances.

## 5 Fits of signal regions

### <sub>76</sub> 5.1 Systematic undertainties

#### 5.2 Results

mass-peak plots)

5.2 Results 24

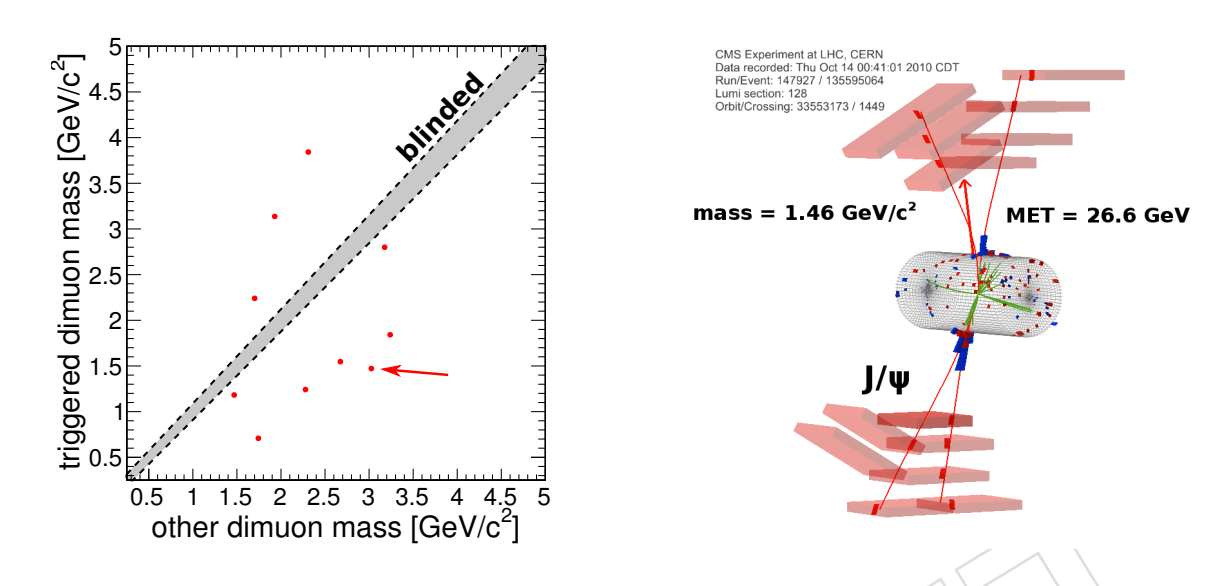


Figure 25: Left: dimuon-dimuon mass plane for signal region (b-1) with the strip along the diagonal blinded (5- $\sigma$  in detector resolution). Right: an event display of a typical event (the one indicated by a red arrow in the dimuon-dimuon plot.)

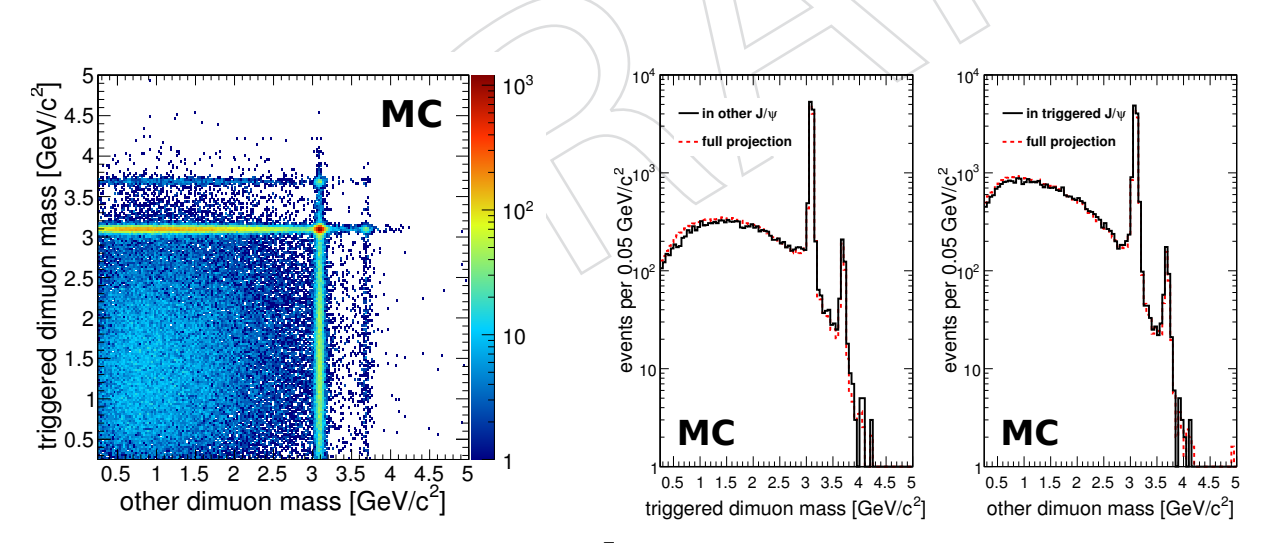


Figure 26: A Monte Carlo simulation of  $b\bar{b} \to 2\mu \, 2\mu \, X$  events to demonstrate the factorization of background mass distributions. Left: the 2-D distribution. Right: projected distributions in a slice around the  $J/\psi$  and the whole distribution, normalized to equal areas.

5.3 Limits **25** 

- 379 **5.3** Limits
- 380 (limit plots)
- **6** Cut-flow and limits on benchmark models
- **7 Conclusions**
- A Motivation for trigger choice

